Entry pupil processing approaches for exo-planet imaging

David C. Hyland*, Texas A&M University, College Station, Texas, 77843-3126

ABSTRACT

In contrast to standard Michelson interferometry, the idea of entry pupil processing is to somehow convert light gathered at each telescope (of a multi-spacecraft array) into data, then process the data from several telescopes to compute the mutual coherence values needed for image reconstruction. Some advantages are that weak beams of collected light do not have to be propagated to combiners, extreme precision relative path length control among widely separated spacecraft is unnecessary, losses from beam splitting are eliminated, etc. This paper reports our study of several entry pupil processing approaches, including direct electric field reconstruction, optical heterodyne systems and intensity correlation interferometry using the Hanbury Brown-Twiss effect. For all these cases and for amplitude interferometry, we present image plane signal-to-noise (SNR) results for exo-planet imaging, both in the case of planet emissions and for imaging the limb of planets executing a transit across their stars. We particularly consider terrestrial-class planets at a range of 15 pc or less. Using the SNR and related models, we assess the relative advantages and drawbacks of all methods with respect to necessary aperture sizes, imager sensitivity, performance trends with increasing number of measurement baselines, relative performance in visible and in IR, relative positioning and path length control requirements and metrology requirements. The resulting comparisons present a picture of the performance and complexity tradeoffs among several imaging system architectures. The positive conclusion of this work is that, thanks to advances in optoelectronics and signal processing, there exist a number of promising system design alternatives for exo-planet imaging.

Keywords: Exo-planets, imaging, interferometry, entry pupil processing, optical heterodyne

1. INTRODUCTION

Concepts for the next generation astronomical facilities seek order-of-magnitude advances in optical angular resolution via long baseline interferometry. This paper concentrates on the design of systems for the detailed imaging of terrestrial-class exosolar planets at distances of up to 15 parsecs. This represents a step beyond the Terrestrial Planet Finder[1-3] (TPF), in that TPF is concerned with resolving a planet on a single pixel to achieve low resolution spectroscopy while nulling the much more intense light of the parent star by the use of either a coronograph or a nulling interferometer. Once TPF identifies interesting planets, the planet imager system considered here can be used to obtain a multi-pixel, multi-spectral image of the planet by means of some form of aperture synthesis. The particular form of the systems we address here involves a collection of separate free-flying, light collecting spacecraft, each one carrying a relatively modest-sized optical or infrared sensor. These spacecraft are accompanied by precisely aligned "combiner" spacecraft that combine pairs of the collector beams, perform starlight nulling and the interferometric measurements needed for imaging. All the spacecraft must fly in precise formation in order to form the image of a very distant object.

In this investigation, we explore possibilities for the reduction of system complexity through the use of novel imaging system architectures that relieve constraints on formation-keeping. Considering the system configuration addressed here, there are numerous inter-spacecraft positioning and system geometry constraints that must be satisfied to assure successful image formation. We summarize each of these constraints, in turn, in the next section and list design alternatives to alleviate the constraint, particularly including the notion of entry pupil processing.

Recently, there has been growing interest in the exploitation of entry pupil processing concepts[4,5] to achieve high resolution optical imaging systems with small to modest sized optical components. "Entry pupil processing" or more popularly, "digitized light" refers to the approach whereby received radiation is converted to data (or down-

* dhiland@tamu.edu; phone 979 862-2647; fax 979 845-6051

Techniques and Instrumentation for Detection of Exoplanets II, edited by Daniel R. Coulter, Proceedings of SPIE Vol. 5905 (SPIE, Bellingham, WA, 2005) · 0277-786X/05/$15 · doi: 10.1117/12.612922

converted to RF) at each of several light gathering devices (telescopes, mirrors, etc.) then the data is processed to synthesize the images. If this can be applied to free-flying formations of telescope-bearing spacecraft such as are considered here, most of the numerous inter-spacecraft positioning and system geometry constraints that must be satisfied to assure successful image formation can be eliminated since one could substitute metrological knowledge for formation keeping control.

Of course, entry pupil processing entails many techniques familiar to radio astronomy. But its application to optics faces several major hurdles, including extremely high frequency signals (hundreds of Terahertz) and quantum noise effects. Advances over the past five years, however, show promise of overcoming these obstacles. First we demonstrate the consistency of the entry pupil processing approach with quantum optics. We survey, in the following section, a variety of techniques, beginning with direct electric field reconstruction methods[6-10] that were originated for quantum control. We then consider, in the fifth section below, the more straightforward optical heterodyning approach. This technique has been applied very successfully by Townes and others[11-13] to interferometry and has gained significant vitality due to very recent advances[14-17] in ultra precise atomic clocks at NIST resulting in femtosecond comb sources. We present our results on sensitivity analysis in to show that under vacuum state fluctuations, heterodyne receivers offer viable signal-to-noise (SNR) for planetary astronomy in the mid-IR range. As a possibility for attaining adequate SNR in the visible range, we explore the concept of ultra-fine resolution imaging of planetary transits. This exploits the particular advantages of heterodyne detection to achieve high signal-to-noise while eliminating the starlight nulling problem as well as rigid geometric constraints on formation control. As the final entry pupil processing technique, we consider use of the Hanbury Brown-Twiss (HB-T) effect[18-21]. We note the relative simplicity of the hardware required for an intensity correlation interferometry array and review recent results for phase retrieval and for imaging SNR. We conclude the paper with overall comparisons of the various techniques with respect to sensitivity, scalability to larger numbers of light collectors and component and system complexities. These assessments are made for cases: Planetary imaging via the planet emissions and imaging of the limb of planets traversing the disks of their parent stars.

2. FORMATION-KEEPING CONSTRAINTS

Figure 1 shows a general architecture, which is consistent with current IR, interferometric, formation flying TPF concepts[1-3], for an exosolar planet imager, including both nulling and imaging components. Regarding the visible, choronograph segment of TPF, one need only replace each of the "nulling pods" in Figure 1 with a single choronograph spacecraft to obtain an imager architecture consistent with the choronograph concept for planet detection. In the following, we comment primarily on the IR architecture shown explicitly in the Figure, but also note the corresponding features of the visible choronograph system.

The precision requirements on formation keeping in the IR case are indicated in the boxes within Figure 1. All the positioning requirements shown have to be maintained within a fraction of a wavelength. The very precise (<1/30 wavelength) positional and attitude adjustments would be made via active optics within the several spacecraft, while the "coarse" adjustments are made through the spacecraft attitude control effectors. Nevertheless, the "coarse" attitude control still requires high precision maneuver control -- typically 1 cm accuracy over 1 to 10^3 kilometers or more baseline. Hence the constraints shown in the Figure are quite severe. The formation-keeping constraints shown in the figure arise chiefly from the exigencies of Michelson interferometry [22]. In the following, we consider each of these constraints in turn.

First consider constraints 1 and 2. To alleviate the precise alignment requirements for space segments within a nulling pod, one might seek suitable optical delay devices that could be hosted within the individual light collector spacecraft. Using relative position data from metrology, these devices could be used to actively correct for positioning errors, even adaptively steering the null of the pod without much accuracy in inter-spacecraft positioning control. With the estimates given in Fig. 1 (with $D_N \approx 100$m) even modest optical delay devices (with 1 to 2m path length) would greatly relieve the formation-keeping constraints. It is desirable to develop delay devices of similar path length that are compact and variable. Besides piezo-driven mirror arrangements, one might consider the use of optoelectronic delay devices. Variable delay devices mounted within the first-level combiners would similarly relieve the need to align them relative to their pod collectors. Thus, progress in relieving constraint 1 would help here as well. Further, if sufficiently large path length delay devices can be developed, it might be possible to eliminate the first-level combiner as a distinct

spacecraft. Light from all of the collectors of a pod would be propagated to one of the collectors and the delays would be used to readjust path length prior to combining the beams.

In the visible choronograph architecture, Constraints 1 and 2 are essentially replaced by the more manageable challenges of apodization and internal alignment precision near the focal plane of the individual light collectors. However, there still remains the need for precise path length control relative to the "second-level" or imaging combiners. Thus, the remainder of our discussion (Constraint 3) applies equally well to the IR or visible imager concept.

With regard to constraint 3, the output beams of the nulling pods (or the individual choronographs) are the initial inputs to the interferometric measurements. To perform these measurements, even without constraints on the

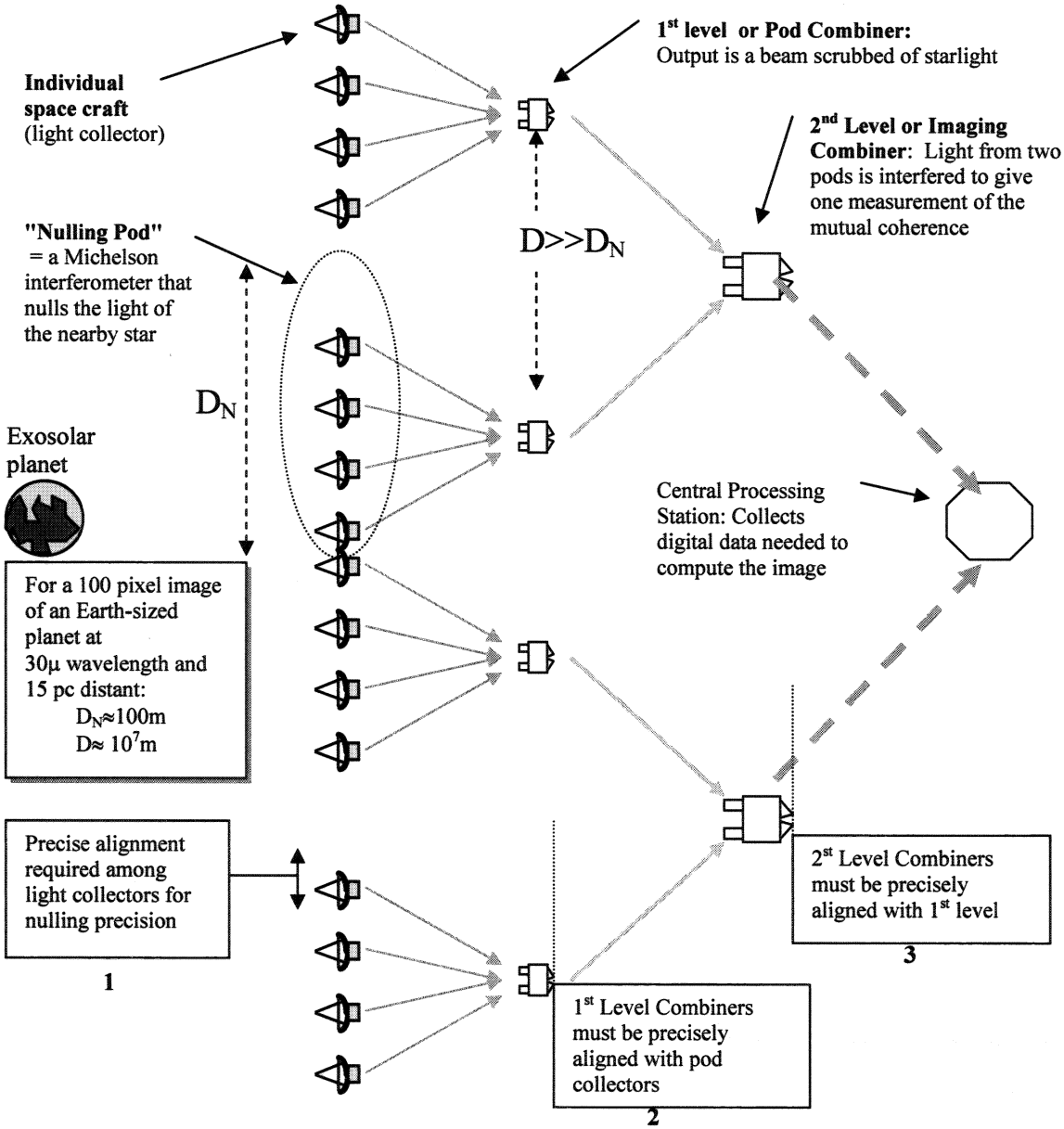

Fig.1: Planet imaging system architecture

relative locations of nulling pods, the second-level combiner spacecraft must still fly in precise alignment with the pair of nulling pods being used. Referring to the estimates in Figure 1, the typical baseline among separate pods could be on the order of 10^7m, so the use of delay devices to alleviate the requirements on second-level combiner positioning or to eliminate the need for such combiners is out of the question. At the same time, with D≈ 10^7m, the conventional approach by which the output beams of two nulling pods are propagated to the second-level combiner, where the beams are physically interfered faces severe challenges because of this propagation distance. It is clear that further alternatives must be explored.

3. ENTRY PUPIL PROCESSING – CONSISTENCY WITH QUANTUM OPTICS

One approach for reducing formation-keeping constraints is to somehow record or reconstruct the electric field of light collected over an appropriate set of entry pupils and then use the electric field data, together with geometric information on the entire entry pupil to compute the desired image. This avoids the physical interference of pairs of collected beams and profoundly alters the system architecture by eliminating all geometric formation-keeping constraints. Apart from the obvious difficulty that optical frequencies are in the range of hundreds of terahertz, one must be concerned with the compatibility of this scheme with quantum optics. In addressing this question, we follow the definitions and notational conventions of Mandel and Wolf [23]. Fig. 2 shows the basic imaging setup.

We wish to reconstruct the intensity distribution deposited by an extended incoherent source on a nearby *image plane*, *I*, using light collected in a set of regions, A_1, A_2, *etc.*, situated on a very distant observation surface, *O*. Let $\mathbf{r}$ and $\mathbf{r}'$ denote the position vectors of points on *O* and *I*, respectively. Consider one polarization state and let *U* denote some component of the electric field of quasi-monochromatic light with mean frequency $\bar{\nu}$. Provided that for all points at which the field is evaluated, the mutual path differences between points within *O* or within *I* are small compared with the coherence length, an approximate expression of the Huygens-Fresnel principle is (see Reference 23, section 4.4.3):

$$U(\mathbf{r},t) = \int_I d^2\mathbf{r}' \frac{e^{ikR}}{R} \Lambda U(\mathbf{r}',t) \tag{1}$$

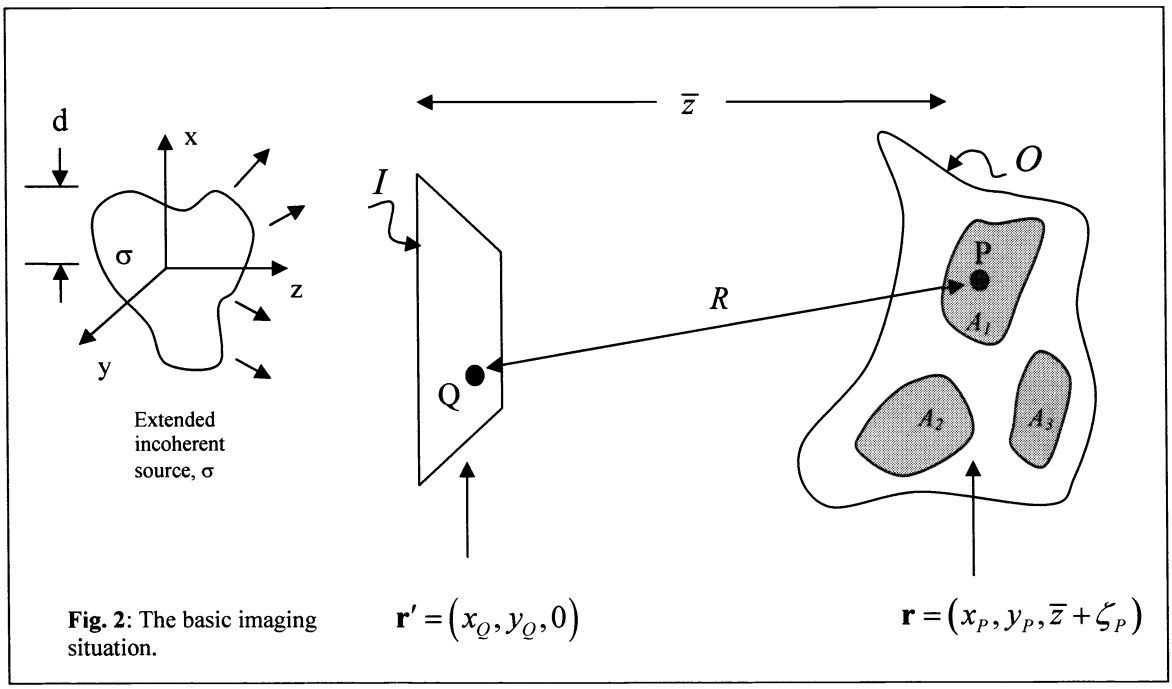

Fig. 2: The basic imaging situation.

apart from a phase factor, where Λ is the inclination factor and k denotes $2\pi\bar{\nu}/c$. To obtain the energy preserving estimate of the inverse of this given that light is collected over a limited entry pupil, one can reverse the time direction in the imaging situation of Fig.2, treating light collectors as projectors, reverse the roles of surfaces *I* and *O* and again apply the Huygens-Fresnel principle to obtain:

$$U^e(\mathbf{r}',t) = \sum_m \int_{A_m} d^2\mathbf{r} \frac{e^{-ikR}}{R} \Lambda^* \; U(\mathbf{r},t) \tag{2}$$

$U^e(\mathbf{r}',t)$ is the field on the focal plane of an ideal optical instrument (consisting strictly of physical optical processing instruments, e.g, lenses, mirrors, beam splitters, etc.) having the specified entry pupil and relying on some photodetection process at the focal plane to acquire the image. Let us call such an instrument a *direct detection* imager. The above classical result carries over into the quantum theory by substitution of the electric field operator, $\hat{U}$ for U (where the notation $(\hat{\bullet})$ distinguishes the operator of an observable from the observed numerical value). Considering the Fock state $|\Psi\rangle$, the energy density accumulated by the direct detector at image plane point $\mathbf{r}'$ over detection time Δt_a is proportional to $I(\mathbf{r}',t)\Delta t_a$, where:

$$\begin{aligned} I(\mathbf{r}',t) &= \langle \Psi | \hat{U}^{e\dagger}(\mathbf{r}',t) \hat{U}^e(\mathbf{r}',t) | \Psi \rangle \\ \hat{U}^e(\mathbf{r}',t) &= \sum_m \int_{A_m} d^2\mathbf{r} \frac{e^{-ikR}}{R} \Lambda^* \; \hat{U}(\mathbf{r},t) \end{aligned} \tag{3.a,b}$$

A slight manipulation gives:

$$\begin{aligned} I(\mathbf{r}',t) &= \sum_{m,n} \int_{A_m} d^2\mathbf{r}_1 \int_{A_n} d^2\mathbf{r}_2 \frac{e^{-ik(R_1-R_2)}}{R_1 R_2} \Lambda_1^* \Lambda_2 \; \mathrm{J}(\mathbf{r}_1,\mathbf{r}_2,t) \\ \mathrm{J}(\mathbf{r}_1,\mathbf{r}_2,t) &\triangleq \langle \Psi | \hat{U}^\dagger(\mathbf{r}_2,t) \hat{U}(\mathbf{r}_1,t) | \Psi \rangle \end{aligned} \tag{4.a,b}$$

Now any one measurement of the observable $\hat{U}^\dagger(\mathbf{r}_2,t_2)\hat{U}(\mathbf{r}_1,t_1)$ is an eigenvalue of the operator. Let us assume that either no two space-time points at which light is collected on the entry pupil are connected by a light cone, or that measurements are made at the same time. In this case (see Reference 23, section 10.8 and equation (10.8-9)) any two vector components of the electric field as measured at two space-time points commute. Also, the spectrum of the electric field is continuously valued. Thus if $|U(\mathbf{r}_1,t_1)\rangle$ and $|U^*(\mathbf{r}_2,t_2)\rangle$ are eigenvectors of $\hat{U}(\mathbf{r}_1,t_1)$ and $\hat{U}^\dagger(\mathbf{r}_2,t_2)$ corresponding to eigenvalues $U(\mathbf{r}_1,t_1)$ and $U^*(\mathbf{r}_2,t_2)$, resp., then $\Gamma(\mathbf{r}_1,t_1;\mathbf{r}_2,t_2) = U(\mathbf{r}_1,t_1)U^*(\mathbf{r}_2,t_2)$ is the associated eigenvalue of $\hat{U}^\dagger(\mathbf{r}_2,t_2)\hat{U}(\mathbf{r}_1,t_1)$. Let $P_{[\Gamma,\Gamma+d\Gamma]}$ be the projector onto the eigenspace associated with all $\Gamma(\mathbf{r}_1,t_1;\mathbf{r}_2,t_2)$ in the range $[\Gamma,\Gamma+d\Gamma]$, where $d\Gamma$ indicates a two-dimensional differential element in the complex plane. Then the probability that $\Gamma(\mathbf{r}_1,t_1;\mathbf{r}_2,t_2) \in [\Gamma,\Gamma+d\Gamma]$ is $dp_\Gamma = \left|\langle \Psi | P_{[\Gamma,\Gamma+d\Gamma]} \Psi \rangle\right|^2$ and (4) may be written:

$$\begin{aligned} I(\mathbf{r}',t) &= \sum_{m,n} \int_{A_m} d^2\mathbf{r}_1 \int_{A_n} d^2\mathbf{r}_2 \frac{e^{-ik(R_1-R_2)}}{R_1 R_2} \Lambda_1^* \Lambda_2 \; \int \mathrm{d}p_\Gamma U^*(\mathbf{r}_2,t) U(\mathbf{r}_1,t) \\ &= \int dp_\Gamma \sum_{m,n} \int_{A_m} d^2\mathbf{r}_1 \int_{A_n} d^2\mathbf{r}_2 \frac{e^{-ik(R_1-R_2)}}{R_1 R_2} \Lambda_1^* \Lambda_2 U^*(\mathbf{r}_2,t) U(\mathbf{r}_1,t) \\ &= \langle U_O^*(\mathbf{r}',t) U_O(\mathbf{r}',t) \rangle \end{aligned} \tag{5.a,b,c}$$

where:

$$U_O(\mathbf{r}',t) = \sum_m \int_{A_m} d^2\mathbf{r} \frac{e^{-ik(R)}}{R} U(\mathbf{r},t) \tag{6}$$

This result for the direct detection imager is identical to that provided by the following procedure: Measure the electric field at all points on the entry pupil (these are all compatible observables), then carry out the computations indicated

above to obtain image intensity at desired points on the image plane. Of course, a further difficulty is that the methods discussed below for measuring or reconstructing the electric field all depend upon some form of photodetection. Thus the measured values are necessarily corrupted by Poisson arrival process statistics in addition to any computational error incurred in carrying out the image reconstruction calculations. Further, since both number and phase are involved in the measurement and these are complementary variables, there is uncertainty principle noise, in other words, vacuum state fluctuations, $\langle vac|\left(\hat{U}(\mathbf{r}_{1,2},t)\right)^2|vac\rangle$, intrude into the image result. The calculation of signal-to-noise (SNR) for all electric field reconstruction methods discussed in this paper is quite involved and cannot be given here. However, the precise results for heterodyne detection are given in References 24-26 where heterodyne detection is contrasted with direct detection in references 24 and 26. A similar SNR calculation for the Hanbury Brown-Twiss approach is given in Reference 27. These results for detection noise are reviewed in later sections below. We anticipate here that in the direct versus heterodyne detection comparison, the sensitivity advantage passes to heterodyne detection in the IR range. A similar conclusion follows for the HB-T approach.. Moreover, when attempting interferometric imaging with simultaneous measurements over a large number, *N*, of apertures, direct detection schemes must split each collected beam into $\frac{1}{2}N(N-1)$ beams with a corresponding diminution of intensity. In contrast for heterodyne detection, as Townes points out, "… such a system involves no further loss in signal-to-noise, because after detection the signal can be amplified and divided without introduction of any significant noise, as is done in radio astronomy."[24] A similar statement may be made for the HB-T technique.

4. PROCESSING APPROACHES: ELECTRIC FIELD RECONSTRUCTION

Beyond the issues considered in the last section, pupil plane processing faces the challenge of electric field measurement despite the extremely high frequencies of optical signals. The work described in this section establishes the very important principle that in fact this challenge can be surmounted. The concept of direct electric field reconstruction entails the transformation of light collected at each of several independent telescopes into Fourier transform data. Such data would be transmitted to some central processing location where the mutual coherence values are computed. In the focal plane optics of each telescope, the incoming beam would be gated to produce a train of brief pulses. The pulsed light is then input to a nonlinear optical device that determines the Fourier transform of each pulse.

The basic operation of most of the techniques surveyed here are as follows. For each pulse, two replicas are generated, each one shifted in frequency relative to one another. Reference 6 reports using a standard 1200-line/mm grating compressor to generate a highly chirped, stretched pulse. The pulses in the test pair are delayed with respect to each other by τ so that each is mixed with a different temporal, and hence spectral slice of the chirped pulse. By interfering the two test pulses, a spectral interferogram, $S(\omega_c)$, is generated and the interferogram is measured with an integrating detector. This yields:

$$S(\omega_c) = \left|\tilde{E}(\omega_c)\right|^2 + \left|\tilde{E}(\omega_c+\Omega)\right|^2 + 2\left|\tilde{E}(\omega_c)\tilde{E}(\omega_c+\Omega)\right| \times \cos\left[\phi_\omega(\omega_c+\Omega) - \phi_\omega(\omega_c) + \omega_c\tau\right] \tag{7}$$

where $\tilde{E}(\omega)$ is the Fourier transform of the pulse electric field, Ω is the spectral shear and ω_c is the variable passband frequency of the spectrometer. While the spectral amplitude is readily obtained, the key contribution is provided by the third term above, which gives the spectral phase in terms of the phase difference between components separated by the spectral shear, Ω. In this way, one obtains spectral phase at a set of discrete frequencies separated by Ω by adding up the phase increments. If the pulse duration is τ_N then the sampling theorem assures us that sampling the spectrum at frequency intervals of $2\pi/\tau_N$ suffices to reconstruct the pulse amplitude and phase.

Originated for the purpose of pulse characterization in quantum control, there are several experimentally tested electric field reconstruction techniques. One principal category is the self- referenced techniques, such as references 6-10, and represented by the SPIDER approach that we have just outlined. These are higher order techniques, that need no independently characterized reference beam in addition to the pulse train to be characterized but utilize signals proportional to the fourth or even sixth power of the input beam intensity. Hence these techniques are not suited to weak

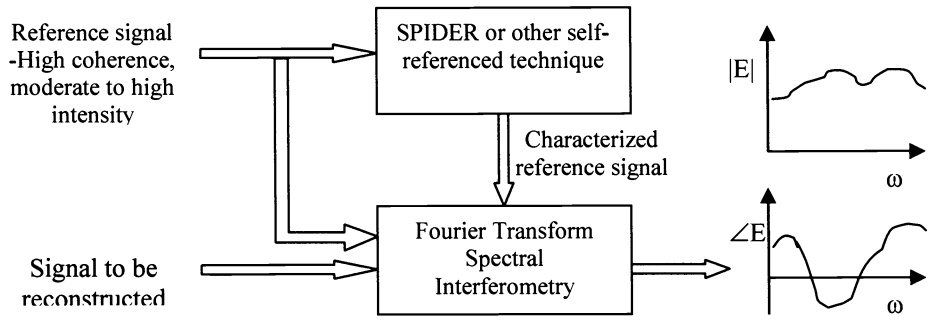

Fig. 3: Combined self-referenced and first-order techniques.

signal intensities. On the other hand, first-order methods such as Fourier Transform Spectral Interferometry [9,10], can cope with weak signals but require a fully characterized reference signal. We would propose to combine the complementary strengths of both methods in manner shown in Fig. 3 to achieve full characterization of low intensity input pulses. The issues of scaling this approach to the application in question, particularly pulse length, and spectral resolution are under study.

5. OPTICAL HETERODYNE RECEIVER

A second fundamental approach to the recording of the electric field for the purpose of pupil plane processing is the notion of heterodyne receivers. Such a development would scarcely have been considered possible before the advent of more powerful optoelectronic technologies. In a key advance, recent developments at NIST and elsewhere as reported by Jones[15], and Cundiff and Hall[16], have produced remarkably stable optical frequency sources based on femtosecond

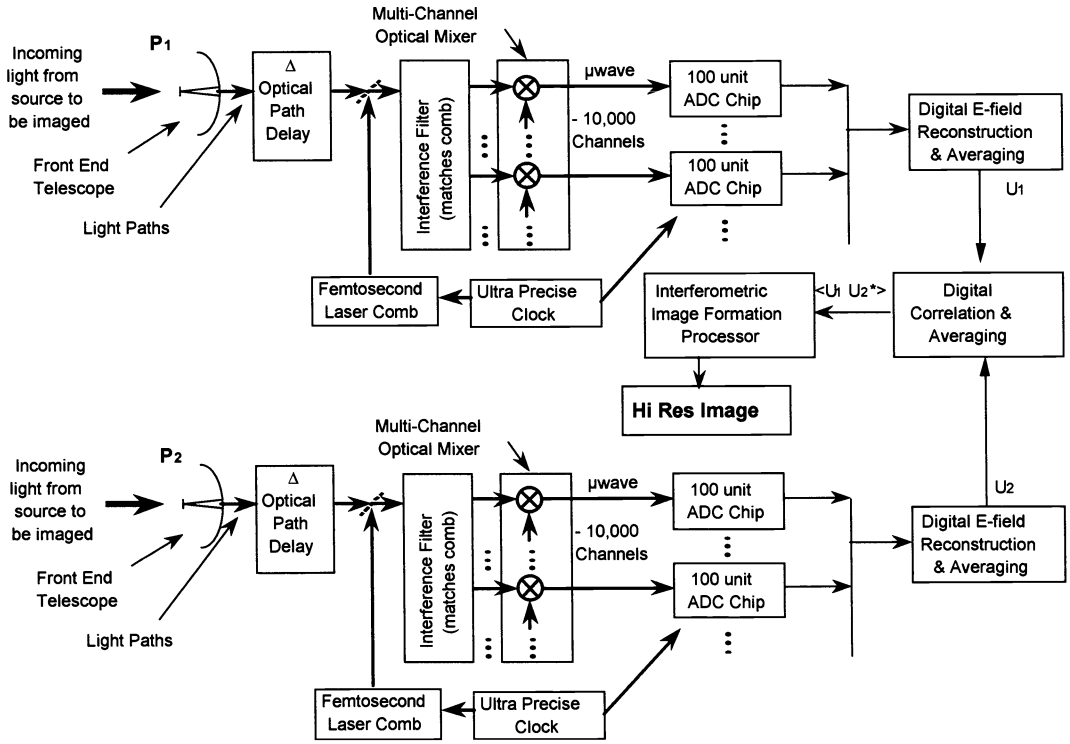

Fig. 4: Optical Heterodyne receiver

mode-lock laser pulsers and nonlinear optical devices. In particular, stable spectral combs of lines separated by microwave-range frequencies have been developed that span an octave or more over the visible or IR frequency range. This device allows one to investigate the design of an optical heterodyne receiver of impressive capability. In the concept depicted in Fig. 4, the light from a source to be imaged is collected in the telescopes at left. An optical delay may be necessary to make gross corrections for the location of the receiver at points P1 and P2. This photon stream is combined with the much stronger light from the femtosecond comb. The comb and incoming light are filtered into some 10,000 bands, (e.g. spanning the visible spectrum) and mixed into 10,000 channels, each some 30 GHz wide. These channels can then be digitized by a bank of analog to digital converters (ADC's) and we have a digital record of the complex E-field observed over the visible band. Very precise clocks are presently available with precision in the range of 10^{-13} (see reference 17). Such clocks allow time synchronization of the observations on separated platforms at P1 and P2. These data are then used to compute values of mutual coherence needed to form an intensity image.

We note that the above receiver design does not necessarily entail the transmission of all ten thousand channels of 30GHz data, only the communication of as many channels as there are wavelength bands of interest for multispectralimaging. For each wavelength band of interest, one would add the outputs of all the heterodyne channels having their frequency bands within the imaging wavelength band, and this would be done at each receiver, before data transmission. After this consolidated output is transmitted to some central computational station and processed through the image synthesis algorithm, the result is the same (apart from quantum noise effects, see below) as would be obtained from the input of electric field measurement data covering the entire imaging wavelength band, which is usually far broader than 30GHz. This can readily be seen from the facts that (1) the analytic signal corresponding to each receiver channel output is merely the frequency down-shifted version of a spectral segment of the incident light and (2) the generalized transform of the analytic signal associated with the incident field has uncorrelated increments. Because of the simplification afforded by this signal consolidation scheme, data rates are manageable, even for spectral resolutions (R=100, say) that are easily high enough to identify most atmospheric constituents.

At this point we must take note of the noise properties of heterodyne reception. The electric field data is extracted from the modulation obtained by combining a frequency slice of the incident field and the field of a coherent source, in this case, the individual "tooth" of the comb source for each receiver channel. The modulation of the combined signal is measured through a photodetection process. The consequence of this is that the receiver channel output is tantamount to the simultaneous measurement of the number operator and a phase operator. Since these do not commute, there is a minimum uncertainty product. The uncertainty principle yields only a lower bound to the quantum noise fluctuations, but a detailed and explicit calculation[11,25] shows that the standard deviation of the noise energy due to uncertainty principle noise accumulated over the detection time is:

$$\left(N_h\right)_{\text{vac}} = h\bar{\nu}\sqrt{\Delta\nu T} \tag{8}$$

where $\bar{\nu}$ is the channel band center frequency, $\Delta\nu$ is the heterodyne sideband bandwidth or the image channel band and T is the postdetection averaging time. Here the "*vac*" subscript reminds us that this is essentially a manifestation of the vacuum state appearing as a contribution to the electric field measurement. It is seen that the number fluctuation variance amounts to one photon for each cycle (at the bandwidth frequency) that occurs over the detection time T.

6. ANALYSIS OF SIGNAL-TO-NOISE FOR HETERODYNE VERSUS DIRECT DETECTION

Now we consider sensitivities of direct detection versus heterodyne detection as judged by the signal-to-noise ratio (SNR), or more precisely the ratio of signal energy collected over the detection time, T, to the standard deviation of the noise energy collected over time T. We make the comparison over the heterodyne channel bandwidths rather than the image wavelength bands, although this tends to the disadvantage of the heterodyne case.

First, considering a single heterodyne receiver and taking account of both vacuum state fluctuations, given by (8.a) and thermal noise, the standard deviation of the noise energy accumulated over the collection time is:

$$N_h = h\bar{\nu}\sqrt{\Delta\nu T\left(1+n_s+\frac{1-\varepsilon}{e^{h\nu/kT_{op}}-1}\right)} \tag{9}$$

Where n_s is the photon number density per mode of the object under study, T_{op} is the temperature of the optics, and ε is the fractional transmission of thermal radiation.

The "signal" energy associated with one mutual coherence measurement is:

$$S_\Gamma = n_s h\bar{\nu}\Delta\nu T \tag{10}$$

Now, the interpretation of the image reconstruction algorithm is that the reconstructed image is the interference pattern on the "dome of the sky" produced by sending all received photons backward, using all telescopes as projectors. The resulting image preserves the total received energy and contains both signal and noise. In particular, noise in the image is precisely the result of the detector noise being propagated backward to be projected onto the dome of the sky. Hence for a single coherence measurement, the total noise energy in the reconstructed image is given above in (9). The "signal" is actually the level of contrast, where a reasonable estimate of total contrast energy over the image is $S_\Gamma - 0$. In summary, the average signal-to-noise over the image plane of a single pair of heterodyne detectors is (see also references 12-13 on the Berkeley infrared Spatial interferometer):

$$SNR_h = \sqrt{n_s^2\Delta\nu T\Big/\left(1+n_s+\frac{1-\varepsilon}{e^{h\nu/kT_{op}}-1}\right)} \tag{11}$$

With this result, we can address multiple heterodyne receivers, let us say one receiver for each telescope in a free-flying formation of separate spacecraft. Suppose we use *N>2* telescopes and use all possible pairs to make mutual coherence measurements. There are thus $\frac{1}{2}N(N-1)$ contributions to the reconstructed image. In view of the interpretation of the reconstructed image, there will be regions wherein the mutual coherence measurement contributions add coherently. Thus an estimate of the image contrast energy is:

$$S_\Gamma = \tfrac{1}{2}N(N-1)n_s h\bar{\nu}\Delta\nu T \tag{12}$$

On the other hand, there are $\frac{1}{2}N(N-1)$ uncorrelated contributions to the image noise energy. Since these must add incoherently, the image noise energy is:

$$N_h = h\bar{\nu}\sqrt{\tfrac{1}{2}N(N-1)\Delta\nu T\left(1+n_s+\frac{1-\varepsilon}{e^{h\nu/kT_{op}}-1}\right)} \tag{13}$$

In summary, taking the ratio of (12) to (13), the average signal-to-noise over the image plane for N telescopes with heterodyne receivers is:

$$SNR_h = \sqrt{\tfrac{1}{2}N(N-1)n_s^2\Delta\nu T\Big/\left(1+n_s+\frac{1-\varepsilon}{e^{h\nu/kT_{op}}-1}\right)} \tag{14}$$

For comparison purposes, we now consider direct detection. In direct detection interferometry, the image contrast energy is *not* $S_\Gamma - 0$ because before photons form interference fringes on photodetectors, each collected beam must be placed through transfer optics in each telescope, then transported to a central collector, then the field patterns of the separate beams manipulated so as to match as closely as possible, all before the beams are combined on the final detector. All of these processes have intrinsic losses. Define:

$\tau_{opt} \triangleq$ fraction of energy transmitted to combiner accounting for losses due to transfer optics and beam propagation to the central combiner (of order 0.05 for systems with many optical components [Townes, ref. 11, p. 1009])

$\mu_f \triangleq$ fraction of energy contributing to interference visibility because of field mismatch and beam misalignment losses (estimated in the range 0.02 to 0.2) (15)

Hence, in this case, the "signal" energy associated with one mutual coherence measurement is:

$$S_\Gamma = \tau_{opt}\mu_f n_s h\bar{\nu}\Delta\nu T \tag{16}$$

Note that the above loss terms do not occur in heterodyne detection since no transfer of collected light is performed, and the receiver picks out precisely the polarization and wavenumber in the incident field that is coincident with the local oscillator.

On the other hand, since the final detection measures combined amplitude and relative phase, i.e. two commuting operators, via a photodetection process, vacuum state fluctuations are not picked up. The contributions to noise are photon arrival fluctuations due to the Poissonian statistics of the target source and thermal noise:

$$N_d = h\bar{\nu}\sqrt{\Delta\nu T\left(\tau_{opt}n_s + \frac{1-\varepsilon}{e^{h\nu/kT_{op}}-1}\right)} \tag{17}$$

Hence, the average signal-to-noise over the image plane of a single pair of telescopes in a direct detection system is:

$$SNR_d = \mu_f\sqrt{\left(\tau_{opt}n_s\right)^2\Delta\nu T\Big/\left(\tau_{opt}n_s + \frac{1-\varepsilon}{e^{h\nu/kT_{op}}-1}\right)} \tag{18}$$

Again consider the use of $N>2$ telescopes in making $\frac{1}{2}N(N-1)$ mutual coherence measurements. As before, we estimate that the image contrast energy is $\frac{1}{2}N(N-1)$ times the maximum fringe energy on each mutual coherence measurement. However in this case, each telescope must divide its beam $N-1$ ways. Hence the energy associated with each measurement is only $\tau_{opt}\mu_f n_s h\bar{\nu}\Delta\nu T/(N-1)$. Thus the image contrast energy is:

$$S_\Gamma = \tfrac{1}{2}N\tau_{opt}\mu_f n_s h\bar{\nu}\Delta\nu T \tag{19}$$

As before, there are $\frac{1}{2}N(N-1)$ uncorrelated contributions to the image noise energy. Hence, the image noise energy is:

$$N_d = h\bar{\nu}\sqrt{\tfrac{1}{2}N(N-1)\Delta\nu T\left(\tau_{opt}n_s/(N-1) + \frac{1-\varepsilon}{e^{h\nu/kT_{op}}-1}\right)} \tag{20}$$

In summary, the average signal-to-noise over the image plane for N telescopes is:

$$SNR_d = \mu_f\sqrt{\frac{\frac{1}{2}N\left(\tau_{opt}n_s\right)^2\Delta\nu T}{\tau_{opt}n_s + (N-1)\dfrac{1-\varepsilon}{e^{h\nu/kT_{op}}-1}}} \tag{21}$$

At this point, we need to account for the manner in which τ_{opt} depends upon the architecture of the direct detection system and its pertinent parameters. Collected light is columnated at each telescope and via a transmitter optic is propagated to a combiner, where a receiver optic intercepts the propagated beam and imparts it to the internal optics of the combiner. We suppose that the transmitter telescope and the receiver both have diameter D_{tr}. Then, if the distance

between collector and combiner is D_B, the fraction of photons leaving the collector that are actually received by the combiner is approximately $\left(D_{tr}^2/\lambda D_B\right)^2 \Big/ \left(1+\left(D_{tr}^2/\lambda D_B\right)^2\right)$, i.e. the solid angle at distance D_B of the receiver telescope divided by the solid angle of the Airy disc of the transmitter telescope. τ_{opt} also includes losses due to incomplete transmission by the various optical components involved in beam splitting. Whether beam splitting occurs at the several collectors or at the combiner, the number of mirrors and/or beam splitters is some multiple of $2(N-1)$. If we scale τ_{opt} by the fractional transmission of a single Bracewell device, denoted by τ_{opt}^0 , we have as an approximate, but relatively optimistic estimate, that $\tau_{opt} \propto \left(\tau_{opt}^0\right)^{N-1}$. Finally, collecting the above results, the approximate model for τ_{opt} is:

$$\tau_{opt} \cong \left(\tau_{opt}^0\right)^{N-1} \left(D_{tr}^2/\lambda D_B\right)^2 \Big/ \left(1+\left(D_{tr}^2/\lambda D_B\right)^2\right) \tag{22}$$

The total throughput for the current dual chopped Bracewell design for TPF-I is less than 8%. Thus a reasonable estimate is that $\tau_{opt}^0 \leq 0.1$. Further, we note that typical collector-combiner distances are driven by image resolution requirements. If we wish to form an image of an Earth-sized planet that is ten pixels on a side, then the maximum baselines of the array must be at least $\cong 10H\lambda/2R_E$, where H is the distance to the target star and R_E is the radius of the Earth. Since the maximum baseline limits the resulting angular resolution, we must use this estimate for D_B in (19):

$$D_B \cong 10H\lambda/2R_E \tag{23}$$

Using (14) and (21-23) we can now contrast the sensitivity performance of heterodyne and direct detection for various scenarios. For example, suppose we are observing an "Earth" with black body IR emission and full daylight reflected light from a black body "sun" at 15 pc. We choose the extremely optimistic values $\mu_f = 0.8, \tau_{opt}^0 = 0.3$ and suppose that $D_{tr} = 1m.$. To achieve any sort of reasonable SNR, we need to postulate 30m diameter telescopes with a 100 hr averaging time. Figure 5 shows SNR estimated for the final image versus wavelength in the 0.1 to 100 micron range for both direct and heterodyne detection. Both cases are evaluated for a spectral resolution of 20. We plot two sets of curves: one pair for imaging with two telescopes and one pair with 20. It is assumed here that starlight nulling has been, somehow, accomplished. Thus SNR losses due to limitations in nulling performance are not accounted for. The figure illustrates that largely due to the loss of signal strength from the beam splitting and beam propagation that must be performed in direct detection interferometry, heterodyne SNR rises much faster with increasing number of apertures. Indeed, for even a modest number of telescopes, the SNR of direct detection begins to decline rapidly. At twenty telescopes, the minimum number needed to obtain 100 pixels in the image, heterodyne detection is comparable to direct detection in the visible band and distinctly superior in the IR range. However, for less than 10 subapertures, only direct detection appears capable of attaining SNR above unity in the visible. This raises the possibility of using a multiplicity of TPF-Coronograph-class spacecraft (together with suitable combiner spacecraft) in a visible-range Michelson imaging interferometer.

While its sensitivity rises quickly with increasing number of apertures, the heterodyne system requires no separate combiner spacecraft as would direct detection. Moreover, with local heterodyne receivers and entry pupil processing, the requirements for sub-micron accuracy in path length control and micro-arc-second pointing control to achieve the needed beam propagation, combination, and field matching over baseline distances of hundreds to thousandsof kilometers, using exceedingly low intensity beams that cannot be amplified are all eliminated. Instead, using the collected and digitized signals and metrology data on relative spacecraft positions, the image synthesis algorithm can be used to reconstruct the image despite any spacecraft positional errors. In other words, one can substitute metrological knowledge for control, thereby substantially reducing system complexity.

For both direct detection and entry pupil processing, metrology requirements are essentially the same. Further, entry pupil processing requires that the time tags of data from separate receivers be synchronized over the correlation time. But this is equivalent to positioning errors of less than a tenth of a wavelength – comparable to positional metrology requirements. However, it appears that the ultra-high resolution atomic clock technology mentioned above in

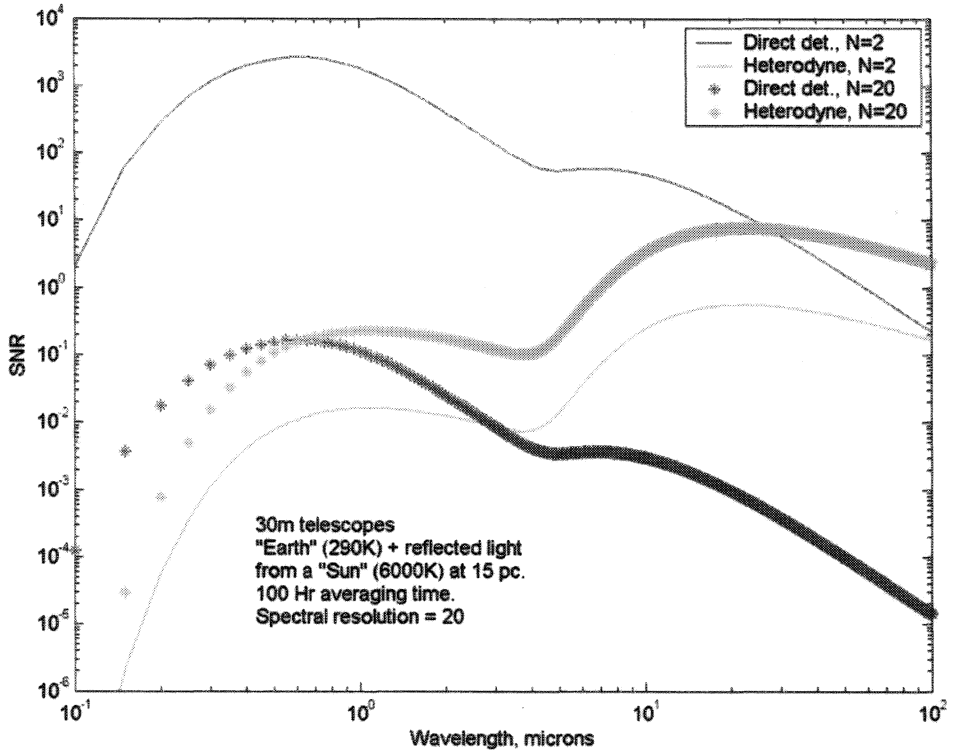

Fig. 5: Image SNR for terrestrial planet viewing at 15 pc.

connection with the femtosecond comb makes the chronography requirements realistic. Note that while the required chronography/metrology system still entails precise spacecraft relative alignment and pointing control to send and collect the requisite optical signals, the optical signals involved are coherent with high SNR, or in the case of optical communication of E-field data, can be amplified and pre-processed.

At this point we must also recognize the discouraging aspects of Figure 5, for both direct and heterodyne detection. First, the photon arrival rate is so small at these distances that neither method is viable in the visible to near-IR range. Indeed, in nighttime conditions the lower wavelength lobes in Figure 5 disappear entirely. Secondly, even in the IR range, while the heterodyne system obtains approximately ten-to-one SNR, both techniques require very large optics and a very lengthy dwell time. Further, all this assumes that the starlight nulling problem is solved. In particular, if nulling is accomplished at the telescope level with a coronograph, telescope diameter is driven by nulling depth and requires at least 40 meter optics to satisfy nulling requirements for a planet > 0.5AU distant from its star at 15pc.

All of these difficulties are due to the low photon count. For high photon counts, heterodyne detection enjoys the added advantage of a significantly reduced SNR degradation due to uncertainty principle noise. These considerations suggest an alternate method of planetary imaging, as discussed in section 8.

7. ALTERNATE EPP TECHNIQUE: INTENSITY CORRELATION INTERFEROMETRY

As an alternative EPP technique, we consider the Hanbury Brown-Twiss effect[18-21]. For this technique, we suppose that the $N>1$ light-gathering telescopes are each equipped with a photodetector and apparatus to record the time histories of the photodetector output signals. We suppose that there are no physical connections among the telescopes, nor is there any propagation of collected light between them, as there would be if the system were a Michelson interferometer. With each telescope operating as an independent unit, photodetector output fluctuations are separately recorded and the data communicated to some convenient location where the cross-correlation statistics of the N signals are computed. From these statistics, imaging or astrometry data are, in turn, computed.

An exposition of the details of this approach are given in Ref. [18-21,27,28]. Here we briefly summarize. Consider two identical telescopes, equipped with identical photodetectors, and denote the two photodetector fluctuations by $\Delta J_1(t)$ and $\Delta J_2(t)$. Define the single-time normalized correlation coefficient:

$$C(d) \triangleq \left\langle \Delta J_1(t) \Delta J_2(t) \right\rangle \Big/ \sqrt{\left\langle \left[\Delta J_1\right]^2 \right\rangle \left\langle \left[\Delta J_2\right]^2 \right\rangle} \tag{24}$$

The essence of the Hanbury Brown-Twiss effect is that:

$$\left|\gamma\left(\vec{\mathbf{r}}_1, \vec{\mathbf{r}}_2, 0\right)\right| \cong \sqrt{\tfrac{1+\delta}{\delta} C_{meas}(d)}, \quad \delta \triangleq \tfrac{1}{2}\eta \left\langle I \right\rangle T_c \tag{25}$$

Where $\left|\gamma\left(\vec{\mathbf{r}}_1, \vec{\mathbf{r}}_2, 0\right)\right|$ is the single time, normalized mutual intensity, η is the detector quantum efficiency, $\left\langle I \right\rangle$ the average intensity and T_c is the correlation time of the collected light. $C_{meas}(d)$ denotes the measured value of $C(d)$, which is obtained by averaging $\Delta J_1(t)\Delta J_2(t)$ over some time period of duration T_a where we assume that this is much larger than the detector response time.

It is necessary to evaluate the statistics of these empirical time averages, particularly the standard deviation of the fluctuations of $C_{meas}(d)$, in order to assess the accuracy of the estimated coherence magnitude. This entails the lengthy calculations given in Reference 28. Here we simply quote the results:

$$\mathrm{SNR}_{|\gamma|} \cong \sqrt{\frac{2\delta^2 \Delta\nu T_a}{1+\delta}}, \ \delta \triangleq \tfrac{1}{2}\eta n_p \tag{26}$$

This is the signal-to-noise ratio of the coherence magnitude measurement. The above expression bears a strong resemblance to the signal-to-noise result derived for an optical heterodyne receiver, where the unity in the denominator arises from vacuum state fluctuations. This should not be surprising since both heterodyne detection and intensity correlation entail measurement of two non-commuting observables and therefore must display uncertainty principle noise. For more than two telescopes, we employ the same reasoning as for heterodyne to obtain:

$$SNR_{HB-T} = \sqrt{\tfrac{1}{2} N(N-1) \delta \eta n_s \Delta\nu T \Big/ \left(1 + \delta + \tfrac{1-\varepsilon}{e^{h\nu/kT_{op}} - 1}\right)}, \quad \delta \triangleq \tfrac{1}{2}\eta n_s \tag{27}$$

Numerically, this result is essentially identical to (21) with (22, 23). Hence the results shown in Figure 5 for heterodyne detection pertain to this technique as well.

As for heterodyne, there is no beam splitting or losses due to transfer optics, so the system SNR grows rapidly with the number of telescopes. Also, knowledge of relative positioning may be substituted for control, but in contrast to the heterodyne approach, highly precise metrology is not needed. This is because we measure magnitude not phase. If one desires an image having N_{pix} pixels on a side then the requirement is that the relative positions of telescopes must be determined to within a sufficiently small fraction of D_b / N_{pix} where D_b is the maximum baseline dictated by the required angular resolution, i.e. $D_b \approx \lambda/\theta_r$ where θ_r is the required angular resolution. For baselines of hundreds of meters, the required precision could be on the order of a meter.

On the other hand, this technique gives the magnitude but not the phase of the Fourier transform of the desired image. In many instances, e.g. when one knows that the background surrounding the target object is black or when one has guide stars in the field of regard when undertaking astrometry, partial information on the image together with magnitude data can suffice to retrieve phase. Thus the image can be reconstructed. The matter of phase retrieval is considered further in Reference 28.

7. PLANTARY IMAGING VIA A HIGH RESOLUTION TRANSIT TECHNIQUE

The above results raise the question: In place of nulling starlight and attempting to detect dim planet light, could we achieve more by forming multi-pixel, multi-spectral images of a planet as it traverses the disc of its star – in other words, *use* (not null) the starlight and image the planet by looking at what is *not* there? Figure 6 illustrates this idea. The transit technique has proved to be a powerful exosolar planet detection technique and is the basis of the Kepler program[29,30]. The basic transit technique is to observe the temporal variations in the white light output of a star. If suitable variations occur, their period and the estimated stellar mass (from luminosity and spectral class) determine the orbit semimajor axis. The relative depth of the variation together with stellar diameter give the planet size and additional data can be gleaned regarding the orbit normal orientation. Of course, only those planets that travel between our position and their parent star can be detected in this way, but existing photometer technology is sufficiently sensitive that high SNR can be achieved at ranges far beyond 15pc.

Here, we take the transit technique a few steps further by using arrays of heterodyne receivers to produce a high resolution image of the star and its interposed planet –as illustrated in the upper left panel of Figure 6. Indeed, the resolution is so fine that we can zoom in on a multi-pixel image of the planet's shadow, as shown in the lower left panel. Each pixel on the rim of the shadow produces a high resolution spectrum (as shown in the lower right panel), which indicates the composition of the atmosphere and surface over a meridian band. This particularly exploits the very high spectral resolution capability of heterodyne detection. Further, as the planet rotates about its axis, we accumulate composition maps over neighboring meridian bands. Eventually, the data can be combined to produce a full map of the planetary atmosphere and surface, as depicted in the upper right panel of Figure 6. In this "map' detailed information is conveyed on the spatial distribution of individual chemical constituents.

In this scheme, since we are observing absorption spectra, the image contrast energy is proportional to the star's luminance, not to the planetary emissions. This effectively gives us a photon count over a million times larger than was considered in Figure 5. Figure 7 shows SNR calculations for a black body "sun" at 15 pc for direct detection and heterodyne detection with spectral resolution of 20. Because of the much higher photon count, we can assume 1m diameter telescopes and a 300 second averaging time. Again we take the greatly optimistic values $\mu_f = 0.8, \tau_{opt}^0 = 0.3$ for the direct detection case and, of further assistance to direct detection, retain the assumption of 1m diameter transfer optics. Despite these assumptions, heterodyne is comparable to or superior to direct detection (owing to the higher photon count), particularly for the larger number of apertures. Moreover, for the 20 telescope case, heterodyne achieves approximately 100 to 1000 SNR over the near- to mid-IR range using only 1 meter diameter telescopes with the five minute dwell time. This suggests that high resolution imaging of exosolar planets can be accomplished by a formation consisting of independent and nominally identical Kepler-class spacecraft.

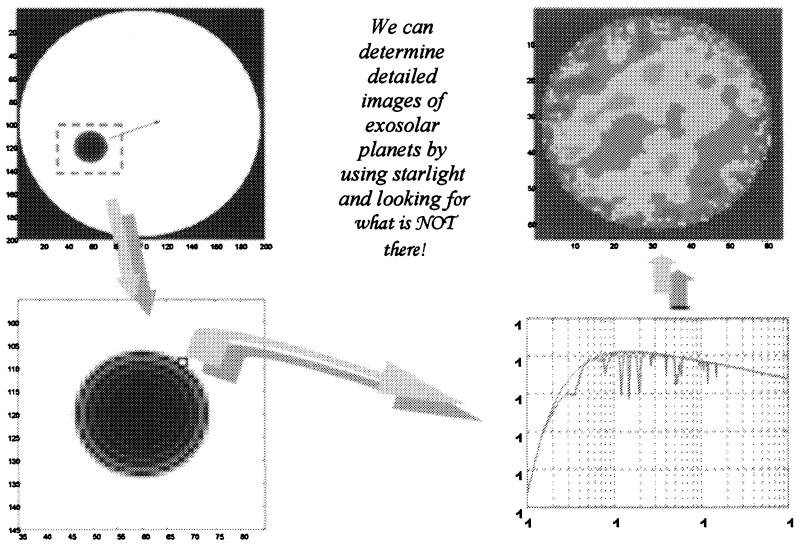

Fig. 6: Illustration of planet imaging via high resolution imaging of a transit event.

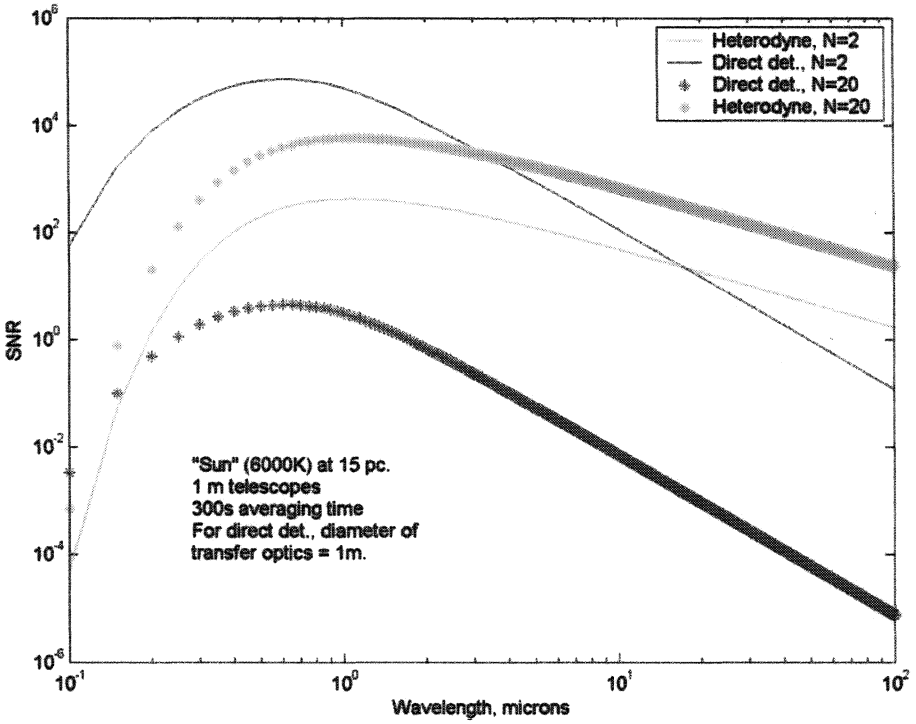

Fig. 7: Image SNR for viewing of a terrestrial planet traversing the disk of its parent star.

8. COMPARISON OF TECHNIQUES AND CONCLUSION

Here we summarize our observations with respect to amplitude interferometry and two of the entry pupil processing techniques. These three technologies are compared for the case of imaging via planet emissions in Table 1 and for the case of imaging planetary transits in Table 2. We offer some overall comments, focusing attention on IR.

Amplitude interferometry offers the highest sensitivity for a single pair of telescopes or nulling assemblies and the only suitable method for starlight nulling which is needed for detection using planet emissions. While detector sensitivity is greatest for a single pair of telescopes, an amplitude interferometry system suffers severe signal losses for a multiple telescope system having numerous pairs (assuming all available pairs are used for coherence measurements). For N telescopes, each of the collected beams must be split $(N-1)$ ways, and each split beam propagated over long distances and then further attenuated by transfer and combiner optics. These effects can conspire to make the overall SNR decline past a certain point as the number of sub-apertures is increased. In addition, amplitude interferometry requires relative positioning control and relative position measurement to within a small fraction of a wavelength. This is a complex and expensive challenge.

In the multi-channel heterodyne technology, the sensitivity of a single receiver is impaired by vacuum state fluctuations, although this can be mitigated by the use of squeezed light from the local oscillator. For a larger number of telescopes and receivers, on the other hand, the signal does not suffer further attenuation since beams are not split and do not traverse transfer optics. Thus the SNR strongly increases with the number of telescopes. A system of 10-20 modest-sized telescopes (<1m diameter) would provide good SNR for such tasks as imaging the disk of a planet as it transits the face of its star or using astrometry data to detect faint planetary companions. Further, extreme precision in controlling relative positions is not needed since these errors can be compensated in the image computation phase if there is adequate metrology. However, the requirements on relative positioning knowledge are just as stringent as for amplitude interferometry.

Table 1: Comparison of Approaches for Terrestrial planet Imaging – Via Planet Emissions

Coherence Measurement technique	Individual Detector Sensitivity	Telescope diameter needed for SNR_{max} =10, T_{dwell}=100hr	Image SNR trend with no. of telescopes	Adequate SNR in Visible?	Adequate SNR in IR?	λ/30 relative positioning control?	λ/30 relative position measurement?
Amplitude interferometry with direct detection	Highest sensitivity-no uncertainty noise	30m	⇓	Possibly for < 10 subapertures	Not for more than ten sub-apertures	Yes.	Yes.
Heterodyne detection + entry pupil processing	Less: Sub-Poissonian SNR due to uncertainty noise	40m	⇑	No..	Yes.	No.	Yes.
Intensity correlation interferometry with phase retrieval	Nearly identical to heterodyne	40m	⇑	No.	Yes.	No.	No. Position knowledge accuracy

Table 2: Comparison of Approaches for Terrestrial Planet Imaging – Planetary Transit Events

Coherence Measurement technique	Individual Detector Sensitivity	Telescope diameter needed for SNR_{max} ***=1000*** ***T_{dwell}=5min***	Image SNR trend with no. of telescopes	Adequate SNR in Visible?	Adequate SNR in IR?	λ/30 relative positioning control?	λ/30 relative position measurement?
Amplitude interferometry with direct detection	Highest sensitivity-no uncertainty noise	<1m	⇓	No.	No.	Yes.	Yes.
Heterodyne detection + entry pupil processing	Less: Sub-Poissonian SNR due to uncertainty noise	1m	⇑	No.	Yes.	No.	Yes.
Intensity correlation interferometry with phase retrieval	Nearly identical to heterodyne	1m	⇑	No.	Yes.	No.	No. Position knowledge accuracy

The Hanbury Brown and Twiss (HB-T) technology, in contrast to the relatively complex and expensive heterodyne receiver technology, requires only a photodetector at each telescope and means to communicate and process the collected data. The output from each photodetector, possibly after low-pass filtering, is transmitted to a suitable location where the cross-correlations among all pairs of photodetector fluctuations are computed. By virtue of an essentially non-classical, quantum effect, these cross-correlations are proportional to the square of the magnitude of the coherence. Hence, one obtains the magnitude of the Fourier transform of the desired image. In many instances, partial information on the image together with magnitude data can suffice to retrieve phase. Thus the image can be reconstructed.

The sensitivity of HB-T for a single baseline is nearly identical to heterodyne. As for heterodyne, there is no beam splitting or losses due to transfer optics, so the system SNR grows rapidly with the number of telescopes. Also, knowledge of relative positioning may be substituted for control, but in contrast to the heterodyne approach, highly precise metrology is not needed. The required relative position knowledge is a small fraction of the maximum baseline divided by the number of pixels on a side of the desired image. This required precision can be on the order of a meter to tens of meters.

Thus, perhaps surprisingly, the HB-T technique appears to offer the greatest all-round capability for the minimum complexity and cost. To summarize the advantages:

- The light collecting telescopes are completely independent, not even the propagation of collected beams to some central combiner is needed. Only the *data* on the several photoelectric signals are brought together.
- As a consequence, the optical path differences do not have to be maintained strictly constant and slight optical element motions have a very small effect.
- The requirements on the *a priori* knowledge of the relative positions of the telescopes are extremely benign as noted above.
- System sensitivity improves rapidly with the number of telescopes. There are no losses due to propagation of weak signals or the splitting of beams.
- Finally, the light-collecting telescopes need not be of very high optical quality, since their chief function is merely to direct the light to a photodetector at the focus.

REFERENCES

1. "Terrestrial Planet Finder", JPL Publication 99-3, May 1999, http:/tpf.jpl.nasa.gov/library/tpf_book/index.html.
2. Oliver Lay and Serge Dubovitsky, "Architecture Selection and Optimization for Planet Finding", SPIE Confernece, Glasgow, 2004.
3. Brent Ware, "Observatory Simulation and PSE Summary", Part 16, Proc. TPF-I SWG Meeting #1, March 9-11, 2005.
4. L. D. Millard and D.C. Hyland, "Simplifying Control of Interferometric Imaging Satellite Formations: Benefits of Novel Optical Architectures", AAS paper AAS03-547, American Astronautical Society Conference, Big Sky, Montana, January, 2004.
5. D.C. Hyland, "Image Reconstruction and Image Quality in Formation Control for Space Imaging Systems". International Symposium on Formation Flying, October 29-30, 2002. Centre National d'Etudes Spatiales, Toulouse.
6. C. Iaconis, and I. A. Walmsley, "Spectral phase interferometry for direct electric-field reconstruction of ultrashort optical pulses", *Opt. Soc. Am.,* Jan. 1998.
7. T. I. Kuznetsova and I.A. Walmsley, "Reconstruction of temporal signals from nonlinear optical measurements", *Quantum Electronics,* 28 (8), 728-732, 1998.
8. C. Iaconis, and I. A. Walmsley, "Self-referencing spectral interferometry for measuring ultrashort optical pulses", *IEEE Jour. of Quantum Electronics,* Vol.35, No. 4, April, 1999.
9. L. Lepetit, G. Cheriaux, and M. Joffre, "Linear techniques of phase measurement by femtosecond spectral interferometry for applications in spectroscopy", *J. Opt. Soc. Am. B,* Vol.12, No. 12, December, 1995.
10. C. Dorrer, "Implementation of spectral phase interferometry for direct electric-field reconstruction with a simultaneously recorded reference interferometry", *Optics Letters,* Vol.24, No. 21, November, 1999.
11. C. H. Townes, *J. Astrophys. Astron.,*5, 111, 1984.
12. C. H. Townes et al. Proc. SPIE, 908, 3350, 1998.
13. M. Bester, W. C. Danchi, and C. H. Townes, Proc. SPIE, 40, 1237, 1990.

14. D. D. S. Hale, et al. ApJ, 537, 998, 2000.
15. Jones et al., *Science 288*, p.635, 2000.
16. S. T. Cundiff, J. Ye and J. L. Hall, Optical frequency synthesis based on mode-locked lasers, *Rev. Sci. Insts*., 72, 10,3749-3771 (2001).
17. C. Audoin and B. Guinot, *The Measurement of Time*, Cambridge University Press (2001).
18. Brown, R. Hanbury and Twiss, R.Q.(1956a), *Nature* **177**, 27.
19. Brown, R. Hanbury and Twiss, R.Q.(1956b), *Nature* **178**, 1046.
20. Brown, R. Hanbury, Davis, J. and Allen, L.R. (1967a), *Mon. Not. R. Astron. Soc.* **137**, 375.
21. Brown, R. Hanbury, Davis, J. and Allen, L.R. (1967b), *Mon. Not. R. Astron. Soc.* **137**, 393.
22. A. Quirrenbach, "Optical Interferometry", *Annu. Rev. Astron. Astrophys.* 2001.39:353-401.
23. L.Mandel and E. Wolf, Optical Coherence and Quantum Optics, Cambridge University Press, 1995.
24. C. H. Townes, Noise and Sensitivity in Interferometry, Chapter 4 of: *Principles of Long Baseline Interferometry*. Course Notes from the 1999 Michelson Summer School, August 15-19, 1999, P. Lawson, Ed. JPL Publication 00-009, July 2000.
25. R. H. Kingston, in *Optical Sciences,* Vol.10, ed. D. L. MacAdam (New York: Springer),28, 1978.
26. L. D. Millard and D.C. Hyland, "Simplifying Control of Interferometric Imaging Satellite Formations: Benefits of Novel Optical Architectures", AAS paper AAS03-547, American Astronautical Society Conference, Big Sky, Montana, January, 2004.
27. D.C. Hyland, "Extrasolar Planet Detection Via Stellar Intensity Correlation Interferometry", 35th Colloquium on the Physics of Quantum Electronics, Snowbird, Utah, January 2-6, 2005.
28. D. C. Hyland, "Exo-Planet Detection Via Stellar Intensity Correlation Interferometry, Techniques and Instrumentation for Detection of Exoplanets II, SPIE International Symposium on Optics & Photonics, SPIE paper no. 5905-37, 31 July – August, San Diego, California.
29. Batalha, N. M., Jenkins, J., Basri, G. S., Borucki, W. J., and Koch, D. G., Stellar Variability and Its Implications for Photometric Planet Detection with Kepler, Proc 1st Eddington workshop "Stellar Structure and Habitable planet Finding", Cordoba, 11-15 June 2001 (ESA SP-485, Nov 2001, F. Favata, I. W. Roxburgh & D. Galadi eds)
30. Borucki, W. J., Koch, D. G., Dunham, E. W., and Jenkins, J. M., "The Kepler Mission: A Mission To Determine The Frequency Of Inner Planets Near The Habitable Zone Of A Wide Range Of Stars Planets Beyond The Solar System and The Next Generation of Space Missions", ASP Conf Ser ,119, 153-173 (1997), ed. David Solderblom